https://doi.org/10.1016/j.ijmachtools.2016.12.006 This is the Pre-Published Version.

A novel multi-jet polishing process and tool for high-efficiency polishing

Abstract: Traditional fluid jet polishing (FJP) is limited by its low material removal rate and its applicability to medium-large size surfaces. This paper presents a novel multi-jet polishing (MJP) process and tools based on FJP which can implement high-efficiency polishing on large-scale surfaces or lens array surfaces. The MJP makes use of a purposely designed nozzle which possesses many regularly distributed holes, whose number can be a few to several hundred. Moreover, each hole can spray out a high-energy fluid jet leading to a dramatic increase of material removal. Its feasibility is firstly analyzed through a Computational Fluid Dynamics (CFD) simulation. Hence, its surface generation mechanisms in the integrated polishing mode and discrete polishing mode are studied. After that, a series of polishing experiments on different materials are conducted to validate its polishing performance as compared to single jet polishing (SJP). The experimental results show that the MJP tool can realize a much higher material removal rate, together with compatible surface roughness to SJP. Hence, the MJP tool has the potential to implement high-efficiency polishing on medium-large size surfaces and lens array surfaces.

Keywords: multi-jet polishing, surface generation, computational fluid dynamics, lens array, ultra-precision machining

1. Introduction

With the increasing need for ultra-precision optical components, many sub-aperture polishing methods have been proposed to enhance the polishing efficiency or surface accuracy in recent years. Fluid jet polishing (FJP), proposed by Faehnle et al. [1,2], is one of the promising polishing methods which depends on the pressured mixing of water and abrasive fluid to interact with the workpiece so as to generate material removal. Different from traditional abrasive jet cutting or milling [3-5], the working pressure is relatively low, between 4 bars and 20 bars [6].

Compared with other polishing methods, FJP is a non-contact processing method and has many advantages [7-9], such as high machining accuracy, suitability for polishing various complex surfaces (especially steep, concave aspheric surfaces), undergoes no tool wear and causes no temperature increase of the workpiece during polishing, etc. It has been widely used in polishing optical glass and moulds [8,10], ceramics [11], etc.

However, there still exist limitations of FJP. Low polishing efficiency is one of the main limitations, which affects its application in polishing large size components. Besides, it also takes a relatively long time to polish a small size component as compared to other polishing methods. According to the reported literature, the material removal rate can be increased by increasing the fluid pressure and slurry concentration [7,12]. However, high fluid pressure would lead to a bad surface finish, while high slurry concentration would not only make it difficult to control its stability, but also lead to the congestion of the slurry system. Moreover, the enhancement is limited by only one single jet. Beyond that, Messelink et al. [13] attempted to add pressurized gas into the fluid jet to enhance the polishing efficiency. Though it can increase the material removal rate, the polished surface has deeper surface defects and poorer surface finish than the traditional FJP. Hence, it can only be used in the pre-polishing stage.

High energy cannot be input into a single jet to execute high-accuracy polishing, but it can be distributed to a number of jets with low energy. Cao et al. [14] and Kim et al. [15] assembled a group of jets of atmospheric pressure plasma (APP) together to form an array to treat surfaces more efficiently as shown in Fig. 1(a) and Fig.

© 2016. This manuscript version is made available under the CC-BY-NC-ND 4.0 license http://creativecommons.org/licenses/by-nc-nd/4.0/

1(b). Recently, Pan et al. [16] proposed a method of adopting multi-beam femtosecond laser irradiation combined with acid etching for fast fabrication of a silicon concave microlens array, as shown in Fig. 1(c). Takino and Hosaka [17,18] integrated a number of purposely designed rods in one electrode to implement efficient electrical discharge machining (EDM) of the steel mould surface of lens array, as shown in Fig. 1(d). These methods can be called “Multi Energy Jet Machining”, which are promising and can largely enhance the production efficiency in the industrial field. As for FJP, we could also try to employ a multi-jet tool to replace the single jet tool to enhance the polishing efficiency.

In this paper, a novel MJP tool and method is presented, with the purpose of largely enhancing the polishing efficiency as compared to single jet polishing (SJP), and not degrading its polishing accuracy. The tool design is firstly discussed. Hence, a preliminary study on the feasibility of multi-jet polishing (MJP) through Computational Fluid Dynamics (CFD) is undertaken. After that, the surface generation mechanism of MJP during the polishing process is analyzed, and the surface generation principle in two different working modes is also explored. Finally, experimental verifications are executed on evaluating its technical feasibility as compared to SJP, together with the discussions and conclusions of the paper.

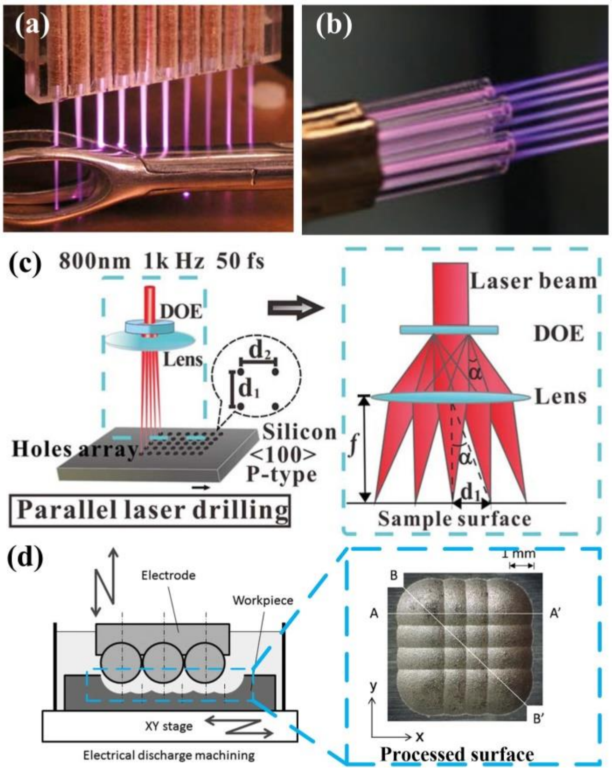

Fig. 1 Examples of multi energy jet machining or processing. (a) Image of ten APP jets processing the surgical tissue forceps surface [14], (b) image of seven well-collimated APP jets [15], (c) schematic diagram of parallel fabrication of a microlens array on silicon using the laser array [16] and (d) principle of multi-rod EDM and the machined surface [18]

2. Design of the MJP tool

Figure 2 shows the schematic diagram of the MJP process. The FJP system can execute both SJP and MJP through the changing of different types of nozzle. The MJP tool is a nozzle with a pattern of holes, or a fixture integrated with many single-orifice nozzles. At present, several kinds of MJP tools have been designed and fabricated firstly for the feasibility study experiments, and three kinds of them are shown in Fig. 3, which are line distributed 5-jet tool (called "LD5JT" for short in this paper), circular distributed 5-jet tool (called "CD5JT" for short in this paper) and square array distributed 9-jet tool (called "SD9JT" for short in this paper), respectively. The MJP tools are made of stainless steel. The diameter of each orifice is designed to be 1 mm, while the distance between each orifice is 2 mm. These MJP tools were purposely designed for the feasibility test experiments.

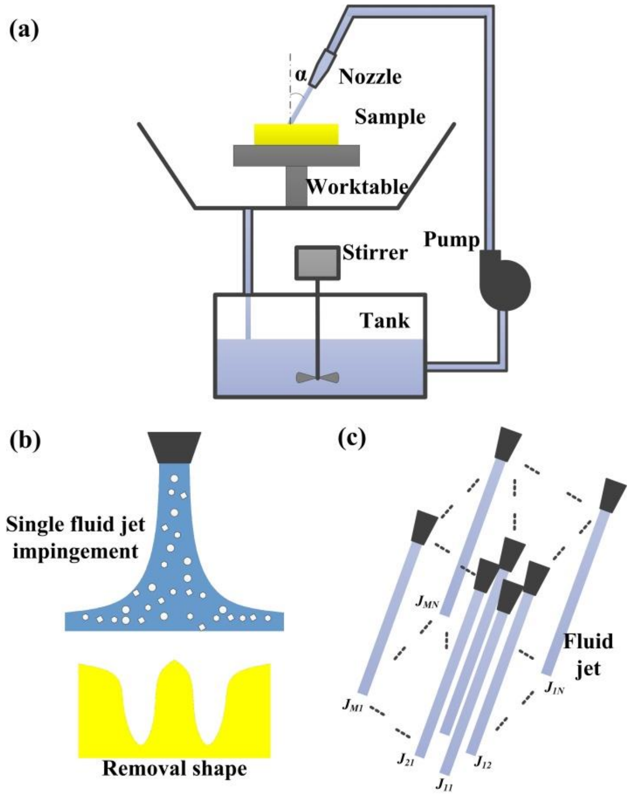

Fig. 2 Schematic diagram of MJP. (a) Composition of the FJP system, (b) single jet impingement and its removal shape, and (c) multi-jet spray

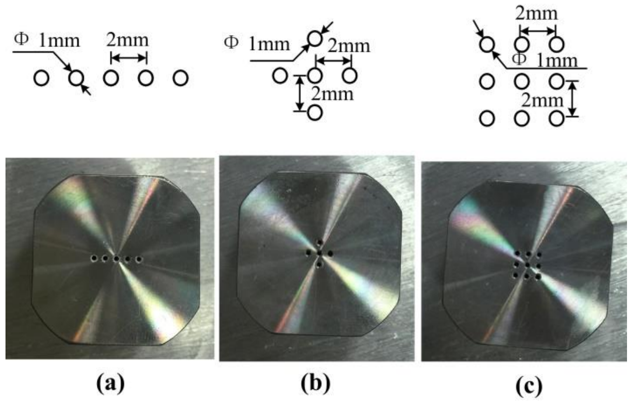

Fig. 3 Three kinds of MJP tools: (a) Line distributed 5-jet tool, (b) circular distributed 5-jet tool, and (c) square array distributed 9-jet tool

3. Feasibility study through Computational Fluid Dynamic (CFD) simulation

3.1 Geometrical modelling

With the increasing computational accuracy of CFD simulation, it has become an effective way in the modelling of FJP. Researchers such as Li, et al. [19], Beaucamp, et al. [6], and Cao, et al. [20] adopted CFD to explain the material removal mechanism or help modelling the tool influence function (TIF). A comparison between SJP and MJP through CFD simulation was firstly carried out to test the feasibility of MJP. The simulation was conducted on nickel copper alloy (NiCu) and BK7 glass, which are ductile and brittle material, respectively. ANSYS FLUENT software was used for numerical simulations. Figure 4 shows the geometrical model of SJP LD5JT polishing and CD5JT polishing. The orifice diameter of all tools is 1 mm, and both the orifice interval in the *x* direction and *y* direction of the MJP tools is 2 mm. The angular Silicon Carbide (SiC) abrasive with the average size of 3.2 μm (wt. 7.7%) was used in this model. The pressure of all inlets was set as 4 bars, and the tool offset was 4 mm. The workpiece material is NiCu alloy which is an important material for the fabrication of optical mould inserts.

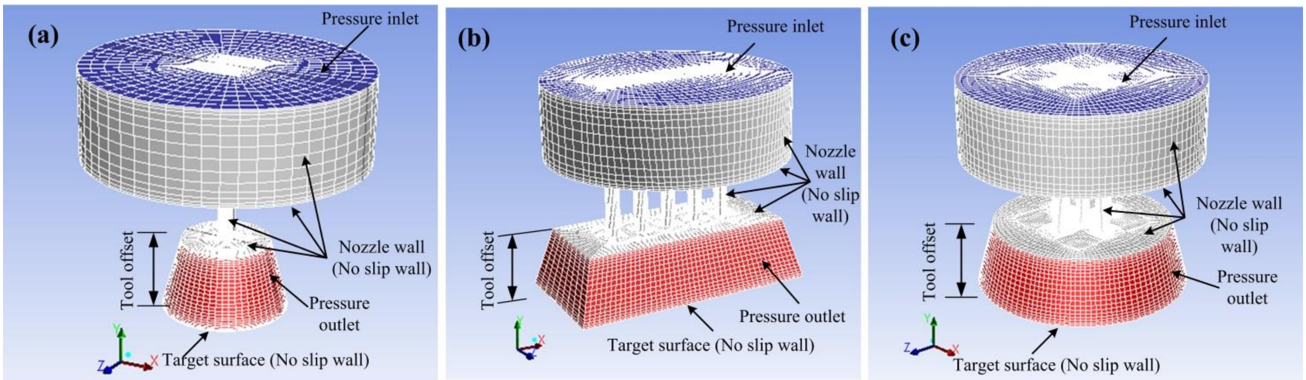

Fig. 4 CFD models: (a) single jet polishing model, (b) line distributed 5-jet polishing model and (c) circular distributed 5-jet polishing model

3.2 Numerical method

The Eulerian-Lagrangian approach is used to simulate the multiphase flow that the liquid water (continuous phase) and abrasive particles (discrete phase) [21] are involved in. In this approach, the water and air are treated as Eulerian phase, and the abrasive particles are treated as Lagrangian phase. Initially, the fluid flow was modelled without the abrasive particles. Afterwards, the discrete phase was used to predict the behaviour of the particle afterwards, following with the erosion calculation.

The volume of Fluid (VOF) model is employed to model the continuous multiphase. A fluid flow solution is obtained by solving the Reynolds average Navier-Stokes equations. The SIMPLE algorithm is employed to solve the pressure-velocity coupling, while the second-order upwind scheme and the second order central-differencing scheme are used for convective and diffusion terms, respectively [22]. Since the shear stress transport k-ω model has superior performance as compared to the k-ε model and has been widely accepted to simulate this kind of model [6,20,23], it is employed in this study to capture the effect of turbulence on the fluid flow.

The simulation of abrasive particle motion is performed using a Lagrangian particle tracking technique. Due to the low slurry concentration used in the FJP process, particle-particle interactions are considered negligible and the particulate phase does not affect the prevailing flow field. Hence, the one-way coupling method is employed. The size of the abrasives was assumed to be the same and uniformly distributed in the fluid slurry. Besides, the material of BK7 glass in fluid jet polishing was assumed to be removed in the ductile mode in this model [20].

The particle might collide with the wall surface and rebound back to the fluid flow domain when moving in the flow system. In this study, the rebound model developed by Grant and Tabakoff [24] is used to determine the particle trajectory and rebound velocity after impact. In this model, the normal coefficient e_n and tangent coefficient e_t are expressed as

$$e_n = 0.993 - 1.76\theta - 1.56\theta^2 - 0.49\theta^3 \tag{1}$$

$$e_t = 0.988 - 1.66\theta + 2.11\theta^2 - 0.67\theta^3 \tag{2}$$

where θ is the impact angle in radians.

Oka's erosion model, which was obtained based on a large number of erosion tests and found to be applicable under any impact conditions and for any type of material [25,26] is used to predict the erosion behaviour when the abrasive impacts the target surface. It is expressed as

$$E(\theta) = g(\theta)E_{90} \tag{3}$$

$$g(\theta) = (\sin\theta)^{n_1}(1 + \mathrm{Hv}(1 - \sin\theta))^{n_2} \tag{4}$$

$$E_{90} = K(\mathrm{Hv})^{k_1}\left(\frac{V_p}{V'}\right)^{k_2}\left(\frac{D_p}{D'}\right)^{k_3} \tag{5}$$

$$n_1 = s_1(\mathrm{Hv})^{q_1}, \quad n_2 = s_2(\mathrm{Hv})^{q_2} \tag{6}$$

where $E(\theta)$ is the erosion damage [mm^3/kg] at an arbitrary impact angle θ; $g(\theta)$ is the impact angle dependence of normalized erosion expressed by the two trigonometric functions and by initial material Vickers hardness number Hv in units of GPa; n_1 and n_2 are exponents determined by the material hardness and other impact conditions such as particle properties, which include particle shape; E_{90} is the erosion damage at normal impact angle; V_p and V' [m/s] are the particle impact speed and the reference impact speed, respectively; D_p and D' [μm] are the particle diameter and the reference diameter, respectively; K denotes a particle property factor such as particle shape (angularity) and particle hardness, which has no correlation among different types of particles and other factors; k_1, k_2 and k_3 are exponent factors, which are affected by other parameters, respectively. As for SiC abrasive, k_2 can be expressed as [26]:

$$k_2 = 3.0(\mathrm{Hv})^{0.085} \tag{7}$$

Table 1 shows the value of the above coefficients and exponents adopted in this study. Table 2 summarizes the workpiece material properties used in this model. The erosion model was defined through a User Defined Function (UDF) in FLUENT software package.

Table 1 Constants and exponents in the erosion model

K	k_1	k_3	s_1	q_1
360	-0.05	0.19	0.71	0.14
s_2	q_2	V' (m/s)	D' (μm)	
2.8	-1.00	99	326	

Table 2 Workpiece material properties used in the simulation model

	Nickel copper alloy	BK7 glass

Density (kg/m^3)	9091	2510
Vickers hardness (Gpa)	1.363	6.166

3.3 Simulation results and analysis

Figure 5 shows the simulation results of the velocity distribution at the cross section of these models and the static pressure distribution after the solution of the continuous phases. The impinging velocity of these models as shown in Fig. 5(a), Fig. 5(b) and Fig. 5(c), are relatively close, including the velocity of each jet in the MJP tool. It suggests that all the particles in the SJP or MJP may have similar impacting velocity to the target surface which may lead to similar material removal. It is interesting to note that there exists flow interference between the adjacent jet, which can directly be reflected in the static pressure distribution as shown in Fig. 5(d), Fig. 5(e) and Fig. 5(f), respectively.

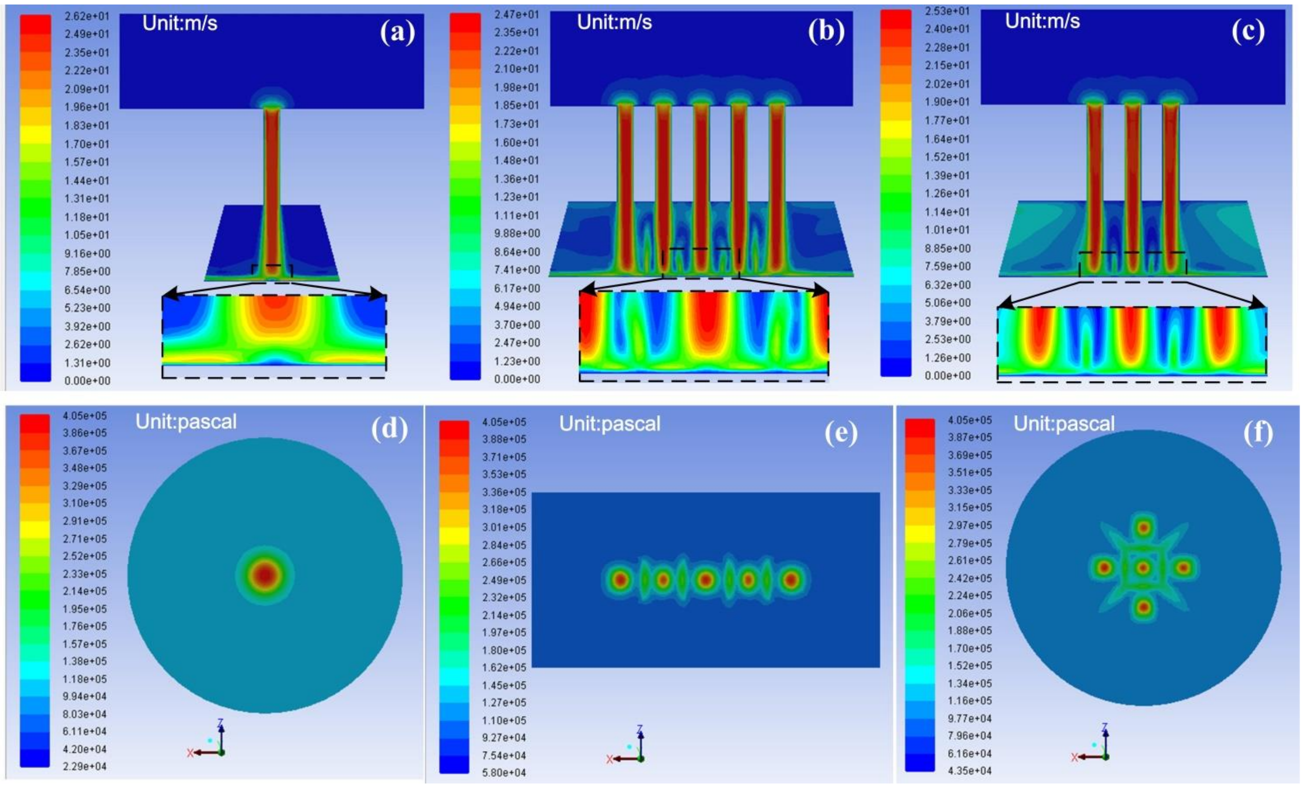

Fig. 5 Simulated fluid velocity distribution at the cross section and the static pressure distribution at the target surface of three different models: (a) velocity distribution in the single jet polishing model, (b) velocity distribution in the line distributed 5-jet polishing model, (c) velocity distribution in the circular distributed 5-jet polishing model, (d) static pressure distribution in the single jet polishing model, (e) static pressure distribution in the line distributed 5-jet polishing model, and (f) static pressure distribution in the circular distributed 5-jet polishing model

Figure 6 shows the target surface erosion rate $R_{erosion}$ [kg/m^2-s], which is defined as [27]

$$R_{erosion} == \sum_{p=1}^{N_{particles}} \frac{\dot{m}_p ER}{A_{face}} \tag{8}$$

$$ER = 1.0 \times 10^{-9} \rho_w E(\theta) \tag{9}$$

where ER [kg/kg] is the erosion ratio which is defined as the amount of mass loss of the target surface material due to particle impacts as divided by the mass of particles impacting; ρ_w is the density of the target surface material which is NiCu; A_{face} [m^2] is the area of the cell face at the wall; $\dot{m}_p$ [kg/s] represents the mass rate of particles impacting the cell surface. As shown in Fig. 6, the erosion rate on NiCu is larger than that of BK7 under the same polishing conditions. The reason is that the hardness of BK7 is higher than that of NiCu. Influenced by the flow interference, the erosion shape of each jet is different from the shape in SJP. However, each erosion shape is basically a ring shape similar to the SJP.

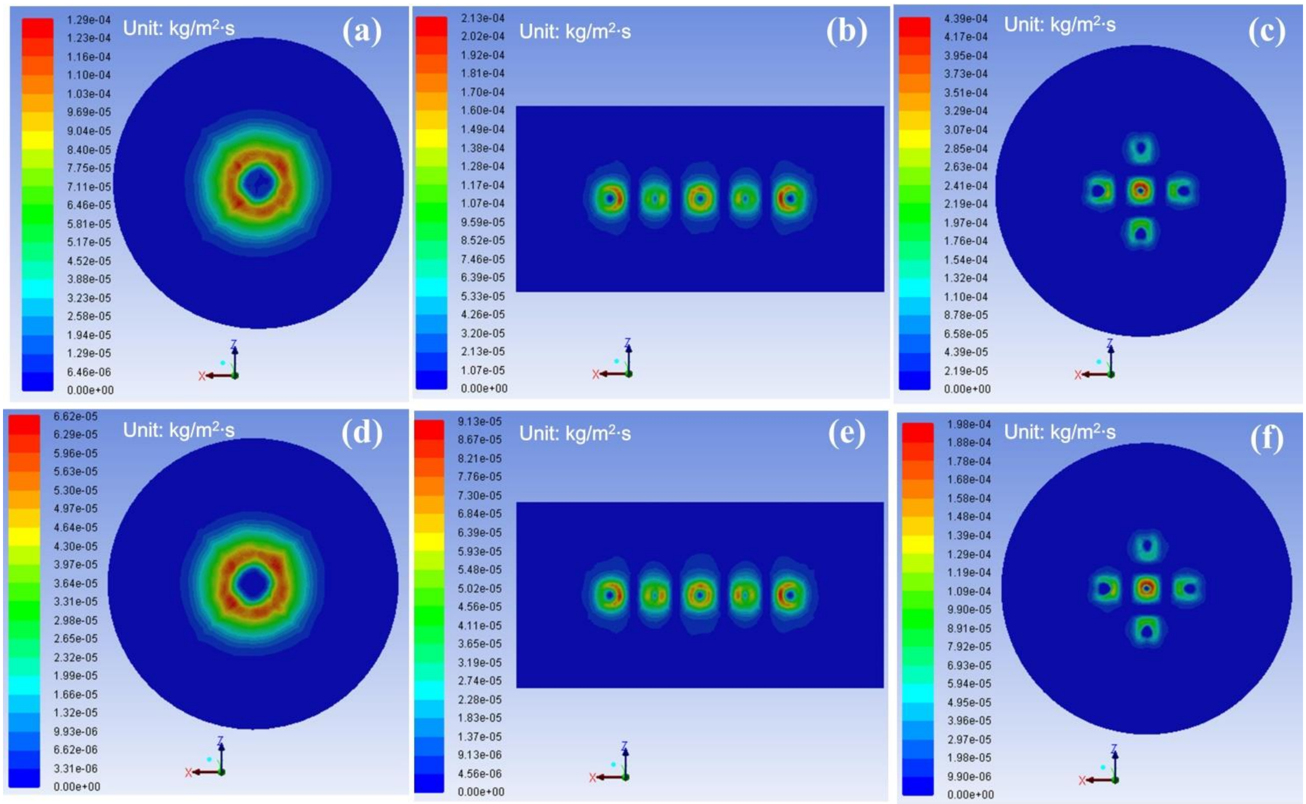

Fig. 6 Simulated erosion rate distribution at the two different target surfaces of three different models: (a) Single jet polishing on nickel copper alloy, (b) line distributed 5-jet polishing on nickel copper alloy, (c) circular distributed 5-jet polishing on nickel copper alloy, (d) single jet polishing on BK7 glass, (e) line distributed 5-jet polishing on bk7 glass, and (f) circular distributed 5-jet polishing on BK7 glass.

With the result of surface erosion rate, the rate of the erosion depth ER_{depth} [m/s] can be deduced through Eq. (10):

$$ER_{depth} == \sum_{p=1}^{N_{particles}} \frac{\dot{m}_p ER}{A_{face}\rho_w} \tag{10}$$

where ρ_w [kg/m^3] is the density of the target surface material. Figure 7 shows the predicted ER_{depth} per minute of these three models according to Eq. (10). The contours of ER_{depth} are shown at the right bottom side of each figure, and the black line inside is the corresponding cross section line. It is interesting to note that the interference of the fluid flow has considerable impacts on the erosion shape. It makes the erosion shape and depth of each jet in the

MJP tool quite different from SJP. For further comparison, table 2 summarizes the average rate of peak removal depth ($PV_{average}$) and volume removal rate (VRR) of each model, which are defined as:

$$PV_{average} = \frac{\sum_{i=1}^{N} PV_i}{N} \tag{11}$$

$$VRR = \iint_{erosion\_zone} ER_{depth}(x, y)dxdy \tag{12}$$

where N is the number of jets in the corresponding model (for instance, N=1 in the model of SJP and N=5 in the model of LD5JT); x and y are the coordinates of the erosion position. As shown in Table 3, it is noted that the $PV_{average}$ in two MJP models are all larger than that for SJP when polishing both NiCu and BK7. This may be caused by two reasons: one is that the superposition of jets in MJP can lead to more material removal; and the other is that fewer abrasives are blocked by the nozzle wall with the MJP tool possessing more jets. Furthermore, VRR of MJP models are also found to be larger than that for SJP even multiplying the corresponding value of N. With these in view, it is believed that MJP may be a feasible way to largely enhance the polishing efficiency as compared to SJP. Hence, a series of MJP tools was designed as shown in section 2 to further validate their feasibility.

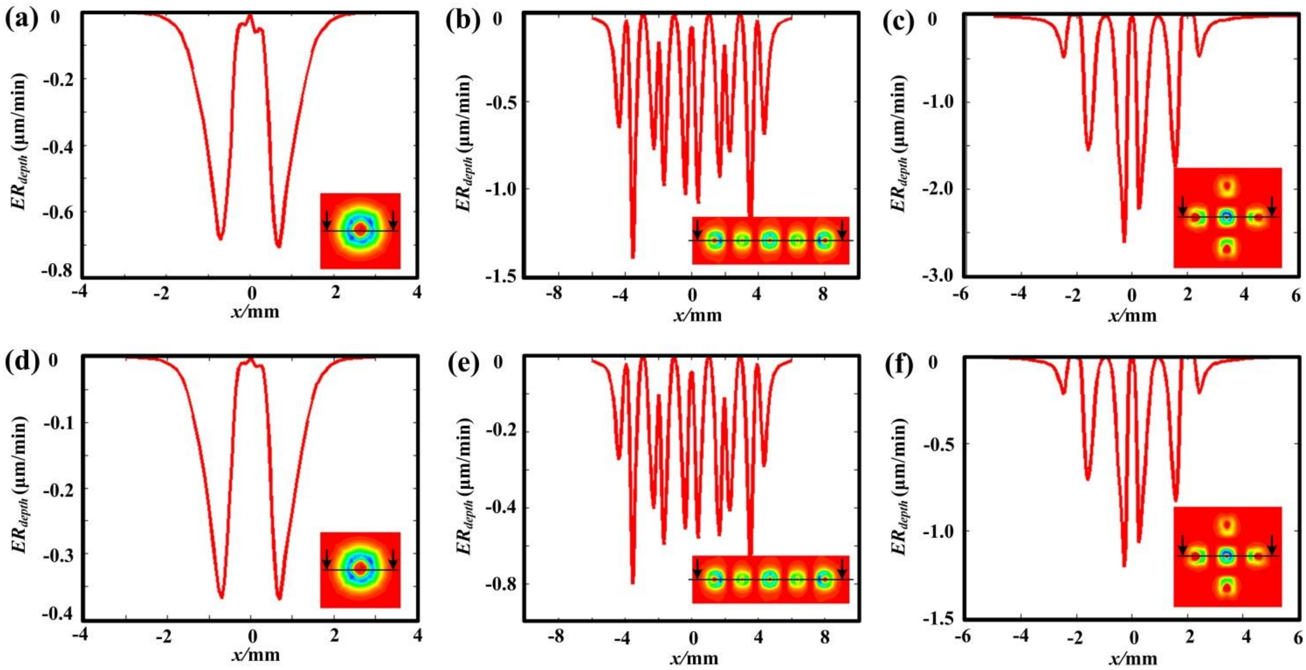

Fig. 7 Predicted rate of erosion depth at the two different target surfaces of three different models: (a) Single jet polishing on nickel copper alloy, (b) line distributed 5-jet polishing on nickel copper alloy, (c) circular distributed 5-jet polishing on nickel copper alloy, (d) single jet polishing on BK7 glass, (e) line distributed 5-jet polishing on bk7 glass, and (f) circular distributed 5-jet polishing on BK7 glass (the negative value means that the material is removed)

Table. 3 Comparison of average peak-to-valley value and volume removal rate of the simulation results

	Average peak-to-valley (μm/min) *		Volume removal rate (mm^3/min)	
	Nickel copper alloy	BK7 glass	Nickel copper alloy	BK7 glass
Single jet polishing	0.6963	0.3698	0.0030	0.0015
Line distributed 5-jet polishing	0.9633	0.4429	0.0162	0.0076

Circular distributed 5-jet polishing	1.3423	0.6213	0.0190	0.0088

*Average peak-to-valley value is defined as a positive value.

4. Surface generation mechanism of MJP

The material removal mechanism of MJP is similar to FJP, which can be explained through the erosion model of the particle/abrasive impinging the target surface. The target surface could be ductile or brittle material. Finnie [28] developed a model for ductile materials, which can explain the erosion well for small impingement angle but has less agreement with the experimental results for large impingement angle. Bitter [29, 30] improved Finnie's model and overcame its limitations. He proposed two types of erosion mechanism for ductile materials: one is due to repeated deformation; the other is cutting wear. Based on the above two models, many investigators optimized the erosion model such as Neilson et al. [31], Hutchings [32], etc.

As for FJP on brittle materials, it is assumed that most material is removed in a ductile way. The ductile erosion mechanism of the brittle materials by FJP has been carried out by Zhu et al. [11] in combination with the erosion experiments. Cao et al. [20] also built a ductile-mode erosion model for the prediction of tool influence function of FJP, which takes into account the effect of the impact velocity, the impact angle, the particle size, the particle shape and the properties of abrasives and targets.

In this study, Oka's erosion model is employed to describe the erosion. In this part, the material removal of MJP is explained in macro scale to demonstrate its surface generation mechanism. For different purposes, the MJP tool works in two different modes which include integrated polishing mode (IPM) and discrete polishing mode (DPM).

4.1 Integrated polishing mode

Figure 8 shows the processing procedure in IPM as compared to SJP. In IPM, the MJP tool is treated as a large polishing tool compared to SJP. The size of the MJP tool's TIF is determined by the number of integrated jets, the size of each jet and the distance between each jet. As shown in Fig. 8, the SJP tool needs to scan a region with the size $P_{x1}\times P_{y1}$ to polish the whole surface, while the MJP tool only needs to scan a much smaller region with the size $P_{x2}\times P_{y2}$. P_{x1}, P_{y1}, P_{x2} and P_{y2} are the length and width of the corresponding scan region, respectively. They can be expressed as:

$$\begin{aligned} P_{x1} &= L - d_{x1}, P_{y1} = W - d_{y1} \\ P_{x2} &= L - d_{x2}, P_{y2} = W - d_{y2} \end{aligned} \tag{13}$$

where L and W are the length and width of the workpiece; d_{x1}, d_{y1}, d_{x2} and d_{y2} are the length and width of the corresponding TIF. It is assumed that $d_{x1}=d_{y1}=d_{x2}=d_{y2}=d$ and $L=W=4d$, and the area of the scanning region of SJP and MJP are $9d^2$ and d^2, respectively. The scanning time is shortened to ~1/9 as compared to SJP, while implementing the same coverage region.

Besides, the jet distribution in IPM can be purposely designed to generate different shapes of TIF. These kinds of TIFs not only enhance the polishing efficiency, but are also adopted to restrain surface errors with various frequencies.

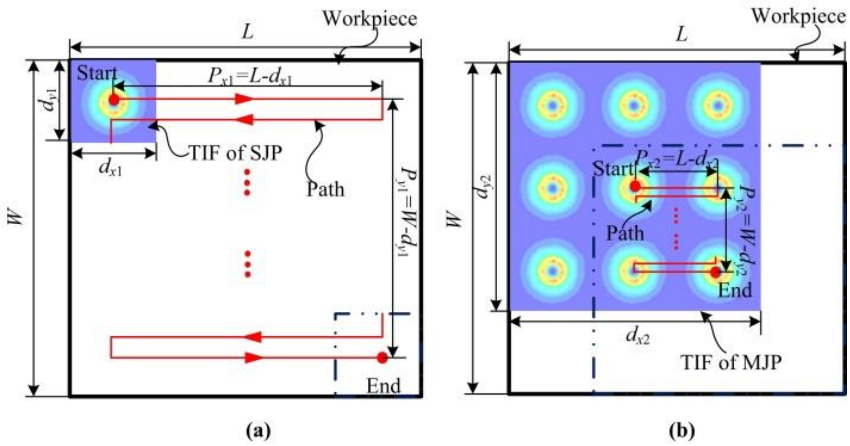

Fig. 8 Comparison between MJP in integrated polishing mode and single jet polishing: (a) Processing procedure of single jet polishing and (b) processing procedure of MJP in integrated polishing mode (the double dot dashed line is the TIF contour at the final path position in the corresponding mode)

In IPM, the material removal $H_{IPM}(x,y)$ can be determined by the 2-dimensional convolution between tool removal function $R_{IPM}(x,y)$ and the dwell time $T(x,y)$

$$H_{IPM}\left(x,y\right)=R_{IPM}\left(x,y\right)*T\left(x,y\right) \tag{14}$$

If the initial surface error data is $Z_0(x, y)$, then the generated surface $Z(x, y)$ can be expressed as

$$Z(x,y)=Z_0\left(x,y\right)-H_{IPM}\left(x,y\right) \tag{15}$$

In abrasive water jet milling process, there exists error induced by the tool overlapping [33,34]. Similarly, this kind of error also exists in FJP, and Cao et al. [35] demonstrated the waviness error arising from the overlapping of the removal profiles based on their model recently. This error can be restrained through decreasing the tool step size and utilizing random tool paths, such as Peano path [36], pseudo random path [37], maze path [38], etc.

At present, FJP has only been used to polish small size surfaces as it is limited by its low efficiency. With the help of MJP in IPM, it is possible to employ the FJP technology for polishing large size surfaces. The size of the nozzle and the number of the jets can be scaled up according to the size of the machined surfaces. Even for large size telescope mirrors, MJP in IPM may also have the potential to be an alternative way to polish them.

4.2 Discrete polishing mode

In DPM, the MJP tool is used to polish lens array surfaces. The jet distribution principle of the MJP tool should be the same as the lens array. For example, if the lens array is distributed in a rectangular pattern, the jet distribution of the MJP tool should also be a rectangular array. And if the lens array is distributed in a honey-comb type pattern, the pattern of the multi-jet distribution should also be the same. In addition, the jet distance should be the same or an integer multiple of the lens unit interval. Figure 9 shows the processing procedure on a 4x4 lens array in DPM as compared to SJP. Traditionally, the lens unit in the array is polished one after another as shown in Fig. 9(a). It is assumed that polishing one unit requires 20 minutes, and thus it takes about 320 minutes to polish all of them. However, if a MJP tool is used, the jet distribution is designed similar to the lens distribution, and all the lens units can then be polished simultaneously as shown in Fig. 9(b). It takes only 20 minutes to polish all of them. Its polishing efficiency is about 16 times increased as compared to SJP.

In this case, a MJP tool can be used with four jets, whose interval is two times larger than that of lens units, and then it takes about 80 minutes to polish all of them as shown in Fig. 9(c). When encountering a lens array with a larger scale, its polishing efficiency can be significantly increased.

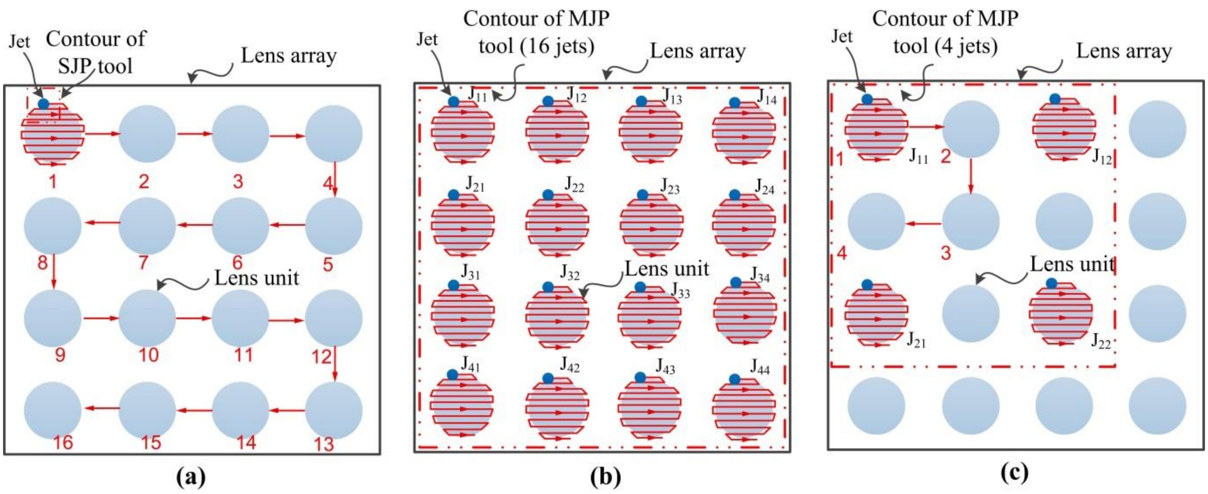

Fig. 9 Comparison between MJP in discrete polishing mode and single jet polishing: (a) Polishing a 4×4 lens array using single jet polishing, (b) polishing a 4×4 lens array using MJP with 16 jets in the discrete polishing mode and (c) polishing a 4×4 lens array using MJP with four jets in the discrete polishing mode

5. Experiments and discussions

5.1 Experimental setup

The experiments were conducted on a *ZEEKO IRP*200 ultra-precision freeform polishing machine. The nozzle and nozzle fixture are changed as shown in Fig. 10. The machine includes three linear axes (i.e. X-axis, Y-axis and Z-axis), three rotational axes (i.e. A-axis, B-axis, C-axis) and one spindle axis, i.e. H-axis. It can perform bonnet polishing and FJP, and has been successfully used to polish ultra-precision optical components such as moulds, prosthetic joints, etc.

Corresponding to the simulation experiment, the workpiece material used in the experiments are NiCu alloy and BK7 glass. The 4000# SiC abrasive combined with water was used as the polishing slurry, with particles of an average size of 3.2 μm.

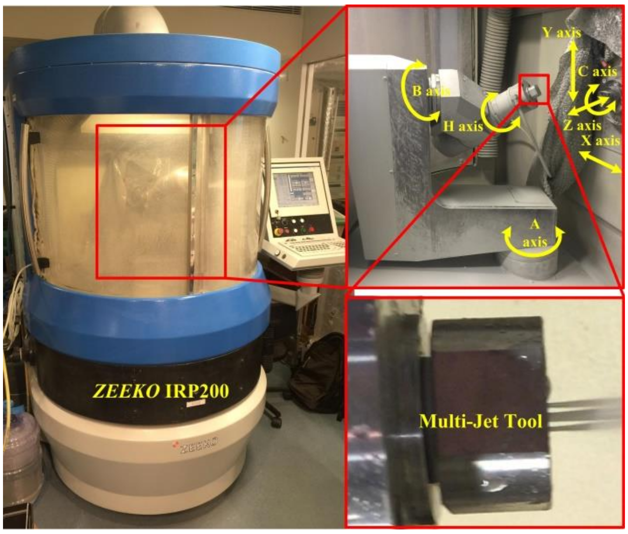

Fig. 10 Photographs of the experimental setup

5.2 Comparison of TIF between SJP and MJP

In order to compare the practical polishing efficiency of MJP and SJP, their TIFs were firstly compared. Three kinds of tools, which are single jet tool, LD5JT and CD5JT, were tested on NiCu alloy and BK7 glass in the experiment. All the experimental conditions were identical to the simulation experiment mentioned in section 3.1. To restrain the influence of the initial surface error, the initial surface of the NiCu alloy samples was diamond turned to attain the form accuracy of 500 nm in peak-to-valley (*PV*), and BK7 glasses were polished firstly with a *PV* value less than 1 μm. The dwell time was 3 minutes to generate the TIF.

Figure 11 shows the 3D TIFs of those tools generated both on NiCu alloy and BK7. It is noted that each jet of the MJP tool generates a ring shape TIF similar to SJP. And the erosion depth of each jet in LD5JT and CD5JT is close to the erosion depth in SJP when polishing the same material. The erosion depth of the cross sections shown in Fig. 11 were also extracted correspondingly, and compared to the simulation results as shown in Fig. 12. Due to the misalignment between the coordinate frames of the measured profile and the simulated profile, the former was registered to the later with the Iterative Closest Point (ICP) algorithm [39]. The top part of each figure in Fig. 12 is the comparison of practical and simulation erosion depth, while the bottom part is the deviation between them. It is noted that the practical erosion depths agree reasonably well with the simulation results. Theoretically, the TIF shape of SJP has a rotationally symmetric ring shape as shown in Fig. 7(a) and (d). But influenced by the cylindricity of the nozzle used in this experiment, the practical generated TIF shape has an incomplete ring shape which is quite obvious in Fig. 11(a) and (d). This is the main reason for the deviation between the simulation and experimental results. Besides, there are some assumptions made in the simulation model mentioned in section 3.2, which also leads to the difference between the simulation and experimental results. The erosion depths of each jet of the MJP tool are close to SJP both in the simulation and experimental results.

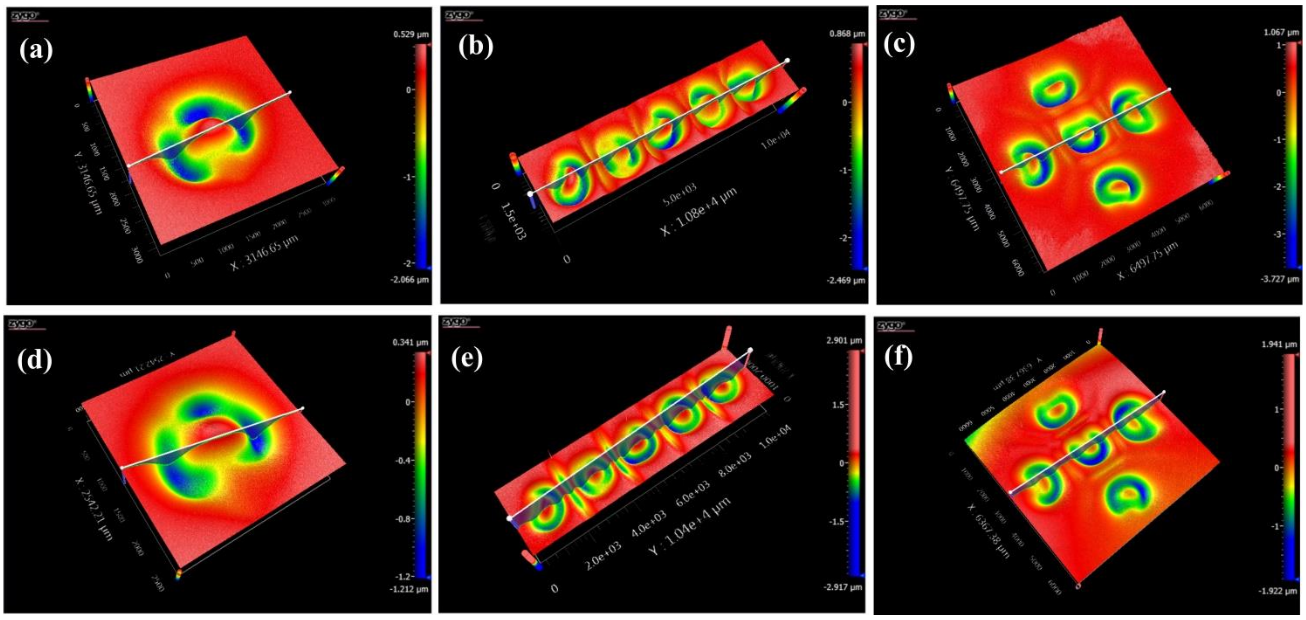

Fig. 11 Tool influence function shapes of different kinds of tools on nickel copper alloy and BK7 glass: (a) Tool influence function of single jet polishing on nickel copper, (b) tool influence function of line distributed 5-jet polishing on nickel copper, (c) tool influence function of circular distributed 5-jet polishing on nickel copper, (d) tool influence function of single jet polishing on BK7, (e) tool influence function of line distributed 5-jet polishing on BK7, and (f) tool influence function of circular distributed 5-jet polishing on BK7

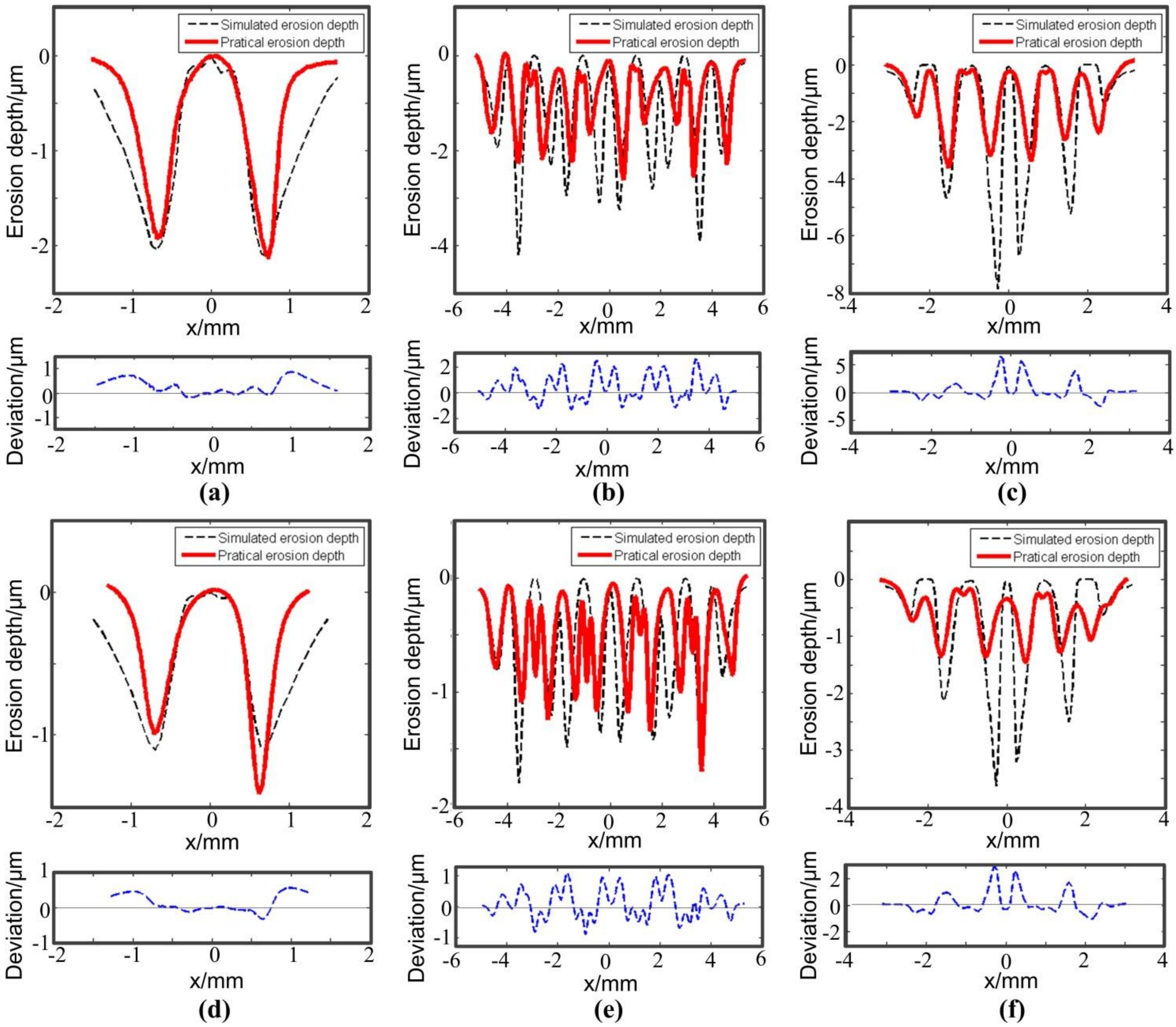

Fig. 12 Comparison of the erosion depth at the cross section between the experiment and simulation results: (a) Erosion depth of the single jet polishing on nickel copper alloy, (b) erosion depth of the line distributed 5-jet polishing on nickel copper alloy, (c) erosion depth of the circular distributed 5-jet polishing on nickel copper, (d) erosion depth of the single jet polishing on BK7 glass, (e) erosion depth of the line distributed 5-jet polishing on BK7 glass, and (f) erosion depth of the circular distributed 5-jet polishing on BK7 glass (the cross sections of them have been shown in Fig. 11)

In order to compare the practical TIFs quantitatively, the $PV_{average}$ and *VRR* of each TIF were also determined and are summarized in Fig. 13. It shows that the $PV_{average}$ of SJP, LD5JT and CD5JT are very close to each other. Moreover, *VRR* of LD5JT and CD5JT are almost equal to or larger than five times the TIF of SJP. Hence, it proves that the MJP tool can prominently increase the material removal rate as compared to SJP. It is also interesting to note that both $PV_{average}$ and *VRR* of CD5JT are larger than those of LD5JT, which also agrees well with the simulation results. It may be caused by the orifice distribution of CD5JT being more concentrated, which makes the energy loss less than LD5JT. The fluid velocity of CD5JT is slightly higher than that of LD5JT as shown in Fig. 5(b) and Fig. 5(c) may be able to explain this phenomenon.

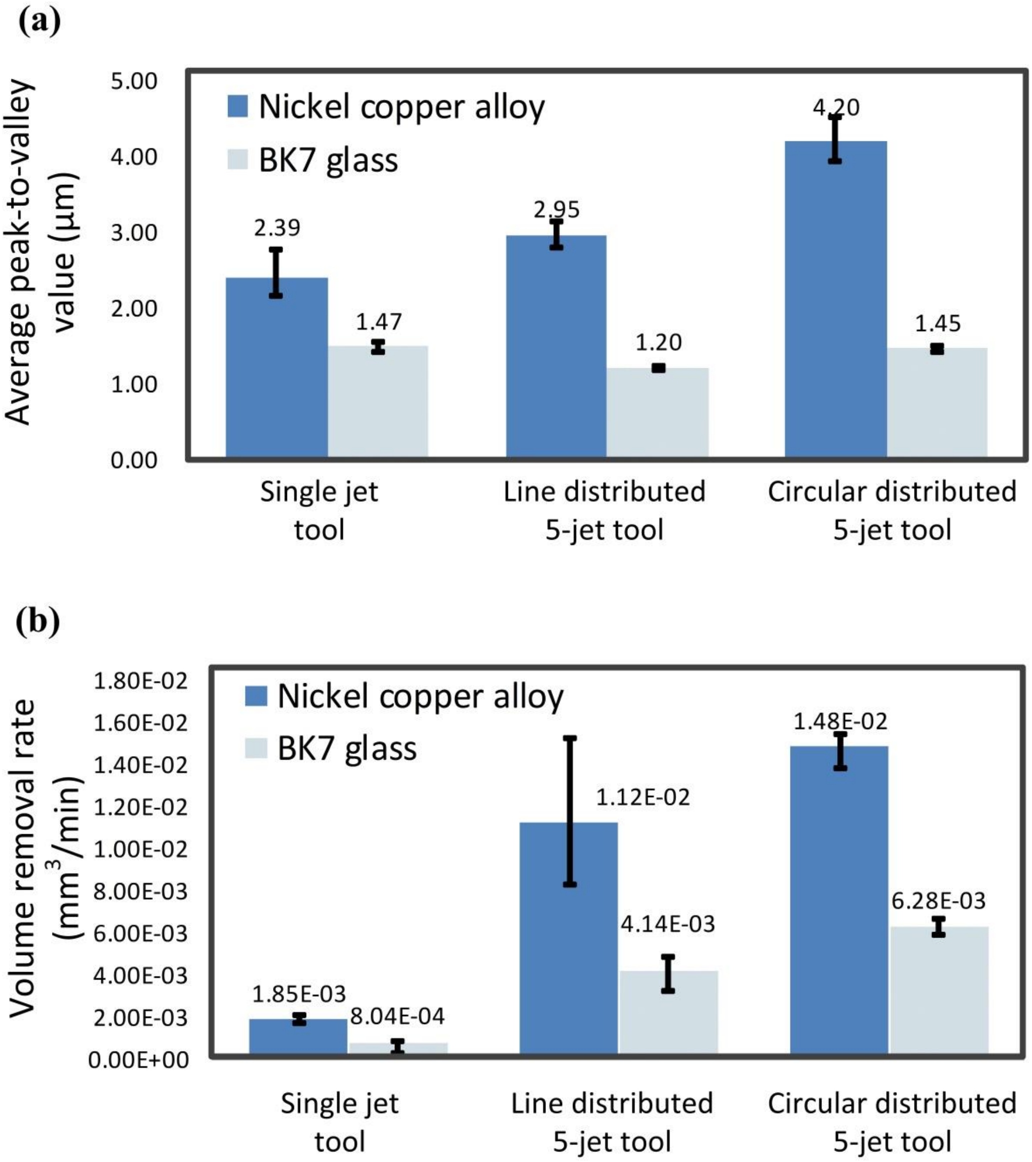

Fig. 13 Comparison of tool influence function characteristics generated by different tools on nickel copper alloy and BK7 glass: (a) Comparison of average peak-to-valley value and (b) comparison of volume removal rate

Moreover, another two kinds of TIFs were also generated: square array distributed 9-jet and 4-jet, respectively. They have different jet intervals: 2 mm for the 9-jet tool and 4 mm for the 4-jet tool. Figure 14 shows the 3D shape of the generated TIF. The influence induced by the interference of each jet as shown in Fig. 5 can be easily observed in Fig. 14(a), which makes the erosion shape of the centre jet different from the external ones. Moreover, the fluid flow interference in Fig. 14(b) is hardly observed as compared to Fig. 14(a) and Fig. 11. The difference of four erosion shapes in Fig. 14(b) is induced by the bad nozzle cylindricity. Hence, when the MJP tool works in DPM as mentioned in section 4.2, the interval between each jet should be designed to be large enough to avoid jet flow interference. On the contrary, the interference of the jets can be used to generate different kinds of TIF shape for different purposes in IPM as mentioned in section 4.1.

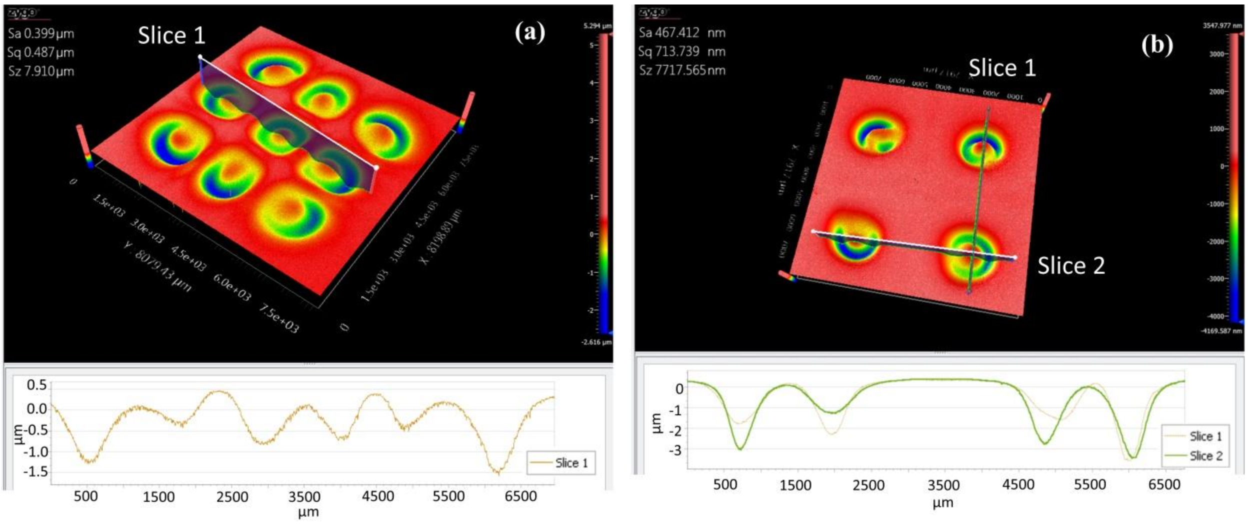

Fig. 14 Tool influence function shape of square array distributed 9-jet polishing and square array distributed 4-jet polishing: (a) Square array distributed 9-jet polishing, and (b) square array distributed 4-jet polishing (the orifice diameter of them are all 1 mm; the jet interval of the 9-jet one is 2 mm, and that of the 4-jet one is 4 mm)

5.3 Comparison of uniform polishing between SJP and MJP

5.3.1 Case 1: Comparison of the generated surface at macro scale

Uniform polishing experiments were conducted to compare the generated surface of SJP and MJP at macro scale. A diamond turned Cu alloy workpiece was used as the testing sample. The polishing slurry was 4000#SiC combined with water, but with the weight ratio of 1kg:10kg. A square array distributed 9-jet tool was employed in this experiment whose TIF has been shown in Fig. 14(a). Table 4 shows the other polishing conditions.

Table 4. Polishing conditions in case 1

<table>
<tr><th></th><th>Single jet polishing</th><th>Square array distributed 9-jet polishing</th></tr>
<tr><td>Fluid pressure (bar)</td><td colspan="2">2.5</td></tr>
<tr><td>Tool offset (mm)</td><td colspan="2">8</td></tr>
<tr><td>Feed rate (mm/min)</td><td colspan="2">10</td></tr>
<tr><td>Scan path</td><td colspan="2">Raster</td></tr>
<tr><td>Scan pitch (mm)</td><td colspan="2">0.25</td></tr>
<tr><td>Scan region (mm^2)</td><td>6×6</td><td>2×2</td></tr>
<tr><td>Practical execution time (s)</td><td>850</td><td>113</td></tr>
</table>

Figure 15 shows the uniform polishing results of the samples. Even though the scanning region of SD9JT is 1/9 of the SJP and the polishing time of the former is ~1/8 of the latter, their polishing regions are almost the same. This indicates that the MJP tool can provide highly efficient coverage of the whole surface during polishing as compared to that for SJP. When polishing large-scale surface, it takes much less time to cover the whole surface through the adoption of the MJP. Due to non-uniform material removal of each jet of the square array distributed 9-jet tool as shown in Fig. 14(a), the uniformity of the polished surface by the MJP tool is not as good as the result of SJP. The reason for the non-uniform material removal of each jet has been discussed in the previous section. If the jet interval is designed to be large enough, each jet of the MJP tool will become independent to generate uniform material removal. Hence, the surface uniformity would be improved. This will be further investigated in future research.

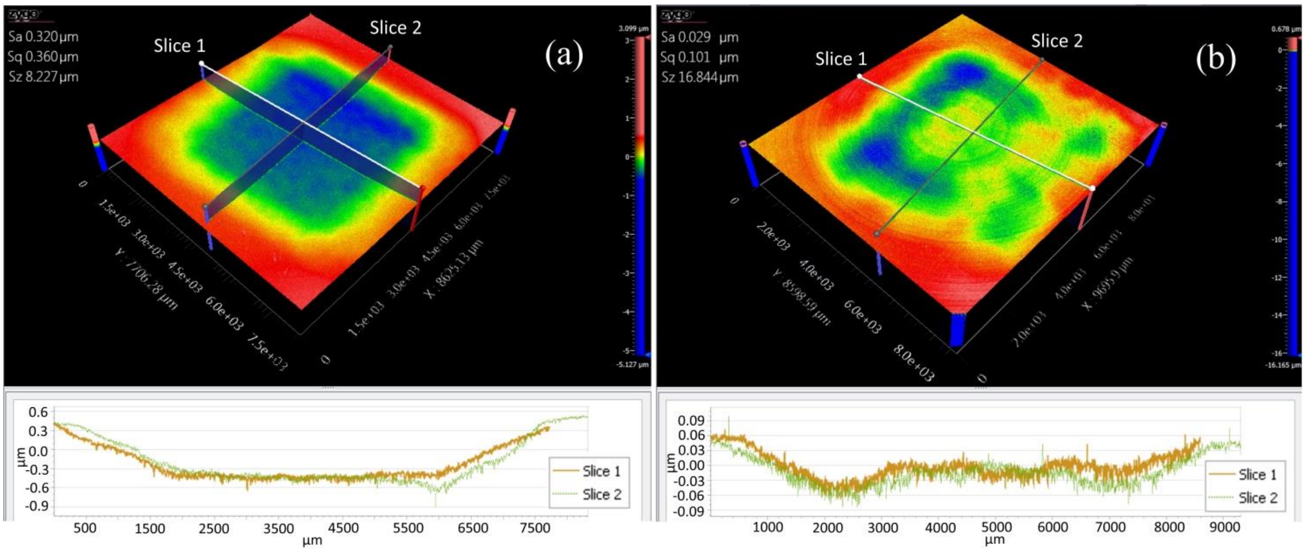

Fig. 15 Surface contours of the polished surface: (a) Polished by a single jet tool and (b) polished by a square array distributed 9-jet tool

5.3.2 Case 2: Comparison of the generated surface at micro scale

To investigate the surface texture polished by MJP, two groups of uniform polishing experiments on NiCu alloy and BK7 were conducted in this experiment. SJP tool and CD5JT were employed. The polishing slurry was the same as in case 1. Table 5 shows the polishing conditions.

Table 5. Uniform polishing conditions on different materials

	Nickel copper alloy		BK7 glass	
	Single jet tool	Circular distributed 5-jet tool	Single jet tool	Circular distributed 5-jet tool
Fluid pressure (bar)	4		4	
Tool offset (mm)	8		8	
Feed rate (mm/min)	20		10	
Scan path	raster		raster	
Scan pitch (mm)	0.25		0.25	
Scan region (mm^2)	8×12		8×12	

Figure 16 shows the AFM measurement results of the workpiece. The surface textures of the same material polished by SJP or CD5JT are almost the same as each other. The arithmetic roughness (Ra) value of them with the same material is also very close as shown in Fig. 16. This further indicates that the material removal mechanism of MJP is almost the same as for FJP. Hence, the MJP can implement high-accuracy polishing as well as SJP. The major difference is the jet interference between the adjacent jets in MJP when the jet interval is small.

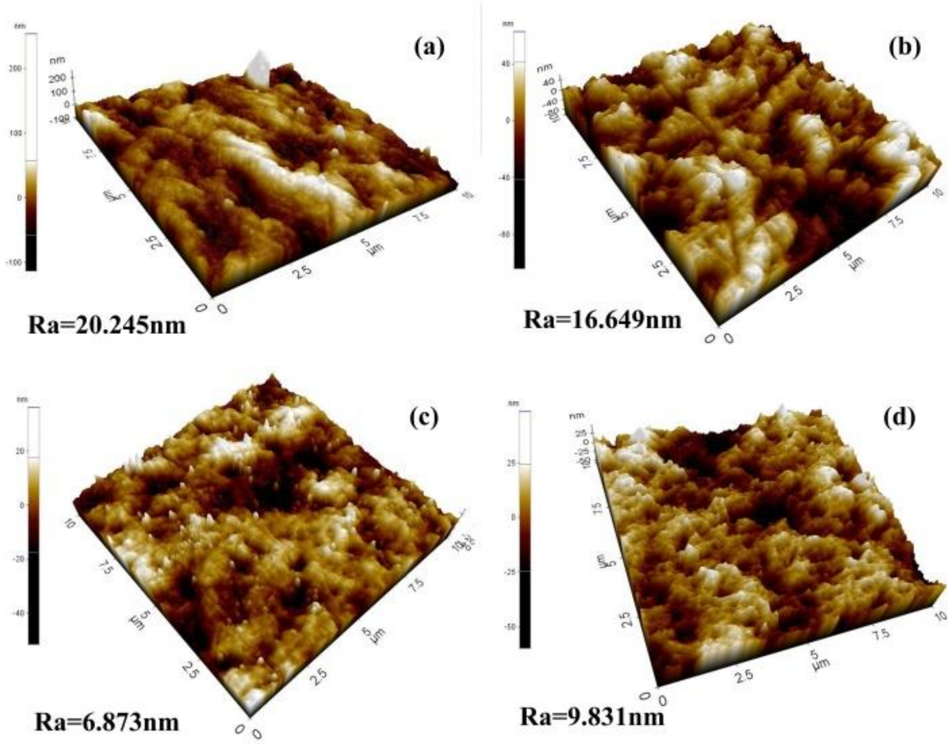

Fig. 16 AFM analysis of the surface texture of different materials polished by different tools: (a) NiCu alloy polished by a single jet tool, (b) nickel copper alloy polished by a circular distributed 5-jet tool, (c) BK7 glass polished by a single jet tool, and (d) BK7 glass polished by a circular distributed 5-jet tool.

6. Conclusion

In this paper, a novel multi-jet polishing (MJP) process and its tool are presented, which attempt to overcome the low efficiency limitation of fluid jet polishing (FJP). The simulation and experimental experiments prove that MJP can provide a much higher material removal rate than that for SJP under the same polishing conditions. Moreover, the size of the MJP tool can be much larger than the SJP tool so as to increase the polishing surface coverage efficiency, which largely enhances the polishing efficiency. Moreover, the surface polished by MJP can achieve a surface roughness which is compatible to SJP. Hence, MJP is becoming a promising method to enhance the polishing efficiency based on FJP. This is particularly true when polishing large surfaces. In addition, it can also be used to provide highly efficient polishing capability for large-scale lens array surfaces through polishing many lens units simultaneously.

However, there also exist challenges of MJP, such as the design and manufacturing of highly erosion-resistant MJP tools, the interference problems of the adjacent jets, etc. These problems will be studied and addressed in future work.

Acknowledgement

The authors would like to express their sincere thanks to the Innovation and Technology Commission (ITC) of the Government of the Hong Kong Special Administrative Region (HKSAR) for the financial support of the research work under the project number: GHP/031/13SZ. They would also like to express sincere thanks to the technical support from Mr. David Lai when performing the experiments.

References

1. O.W. Faehnle, H.V. Brug, H.J. Frankena, Fluid jet polishing of optical surfaces, Applied Optics 37 (1998) 6771–6773.
2. O.W. Faehnle, Shaping and finishing of aspherical optical surfaces, PhD thesis (Delft University, 1998).
3. D.A. Axinte, B. Karpuschewski, M.C. Kong, A. Beaucamp, S. Anwar, D. Miller, M. Petzel, High energy fluid jet machining (HEFJet-mach): from scientific and technological advances to niche industrial applications, CIRP Annals – Manufacturing Technology 63(2) (2014) 751–771.
4. M.C. Kong, S. Anwar, J. Billingham, D.A. Axinte, Mathematical Modelling of Abrasive Waterjet Footprints for Arbitrarily Moving Jets: Part I – Single Straight Paths, International Journal of Machine Tools & Manufacture 53(1) (2012) 58–68.
5. M.K. Kulekci, Processes and apparatus developments in industrial waterjet applications. International Journal of Machine Tools & Manufacture 42(12) (2002) 1297-1306.
6. A. Beaucamp, Y. Namba, R. Freeman, Dynamic Multiphase Modeling and Optimization of Fluid Jet Polishing Process. CIRP Annals – Manufacturing Technology 61(1) (2012) 315–318.
7. S.M. Booij, Fluid jet polishing-possibilities and limitations of a new fabrication technique, Ph.D. thesis (Delft University, 2003).
8. A. Beaucamp, Y. Namba, Super-smooth finishing of diamond turned hard x-ray molding dies by combined fluid jet and bonnet polishing, CIRP Annals – Manufacturing Technology 62(1) (2013) 315–318.
9. F.C. Tsai, B.H. Yan, C.Y. Kuan, F.Y. Huang, A Taguchi and experimental investigation into the optimal processing conditions for the abrasive jet polishing of SKD61 mold steel, International Journal of Machine Tools & Manufacture 48(7) (2008) 932-945.
10. A. Beaucamp, Y. Namba, W. Messelink, D. Walker, P. Charlton, R. Freeman, Surface integrity of fluid jet polished tungsten carbide. Procedia CIRP 13 (2014) 377-381.
11. H.T. Zhu, C.Z. Huang, J. Wang, Q.L. Li, C.L. Che, Experimental study on abrasive waterjet polishing for hard-brittle materials, International Journal of Machine Tools & Manufacture 49 (2009) 569-578.
12. L.T. Ho, Theoretical and experimental investigation of 3D-structured surface generation by computer controlled ultra-precision polishing, Ph.D. thesis (The Hong Kong PolyTechnic University, 2015).
13. W.A.C.M. Messelink, R. Waeger, T. Wons, M. Meeder, K.C. Heiniger, O.W. Faehnle, Prepolishing and finishing of optical surfaces using fluid jet polishing, Optics & Photonics 2005. International Society for Optics and Photonics (2005) 586908-586908-6.
14. Z. Cao, J.L. Walsh, M.G. Kong, Atmospheric plasma jet array in parallel electric and gas flow fields for three-dimensional surface treatment, Applied Physics Letters 94 (2009) 021501.
15. J.Y. Kim, J. Ballato, and S.O. Kim, Intense and energetic atmospheric pressure plasma jet arrays, Plasma Processes and Polymers 9 (2012) 253-260.
16. A. Pan, T. Chen, C.X. Li, X. Hou, Parallel fabrication of silicon concave microlens array by femtosecond laser irradiation and mixed acid etching, Chinese Optics Letters 14(5) (2016) 052201.
17. H. Takino, T. Hosaka, Shaping of steel mold surface of lens array by electrical discharge machining with single rod electrode, Applied Optics 53(33) (2014) 8002-8005.
18. H. Takino, T. Hosaka, Shaping of steel mold surface of lens array by electrical discharge machining with spherical ball electrode, Applied Optics 55(18) (2016) 4967-4973.

19. Z.Z. Li, S.Y. Li, Y.F. Dai, X.Q. Peng, Optimization and application of influence function in abrasive jet polishing, Applied Optics 49 (2010) 2947–53.
20. Z.C. Cao, C.F. Cheung, Theoretical modelling and analysis of the material removal characteristics in fluid jet polishing, International Journal of Mechanical Sciences 89 (2014) 158–166
21. ANSYS FLUENT User's Guide, Release 14.0, Ansys Inc., 2011.
22. A. Mansouri, H. Arabnejad, S.A. Shirazi, B.S. McLaury, A combined CFD/experimental methodology for erosion prediction, WEAR 332-333(2015) 1090–1097.
23. Z. Zhang, C. Kleinstreuer, Low Reynolds Number Turbulent Flows in Locally Constricted Conduits, AIAA Journal 41(5) (2003) 831–840.
24. G. Grant, W. Tabakoff, Erosion prediction in turbomachinery resulting from environmental solid particles, Journal of Aircraft 12(5) (1975) 471-478.
25. Y.I. Oka, K. Okamura, T. Yoshida, Practical estimation of erosion damage caused by solid particle impact. Part 1: effects of impact parameters on a predictive equation, Wear 259 (2005) 95-101.
26. Y.I. Oka, T. Yoshida, Practical estimation of erosion damage caused by solid particle impact. Part 2: mechanical properties of materials directly associated with erosion damage, Wear 259 (2005) 102-109.
27. ANSYS FLUENT Theory Guide, Release 14.0, Ansys Inc., 2011.
28. I. Finnie, Erosion of surface by solid particles, WEAR 3 (1960) 87-103.
29. J.G.A. Bitter, A study of erosion phenomena, Part 1, WEAR 6 (1963) 5-21.
30. J.G.A. Bitter, A study of erosion phenomena, Part 2, WEAR 6 (1963)169-190.
31. J.H. Neilson, A Gilchrist, Erosion by stream of solid particles, WEAR 11 (2) (1968) 111-122.
32. I.M. Hutchings, A model for the erosion of metals by spherical particles at normal incidence, WEAR 70 (1981) 256.
33. J. Billingham, C.B. Miron, D.A. Axinte, M.C. Kong, Mathematical modelling of abrasive waterjet footprints for arbitrarily moving jets: Part II - Overlapped single and multiple straight paths, International Journal of Machine Tools and Manufacture 68 (2013) 30-39.
34. P. Lozano Torrubia, J. Billingham, D.A. Axinte, Stochastic simplified modelling of abrasive waterjet footprints, Proc. R. Soc. A 472 (2016) 20150836.
35. Z.C. Cao, C.F. Cheung, M.J. Ren, Modeling and characterization of surface generation in fluid jet polishing, Precision Engineering 43 (2016) 406-417.
36. H.Y. Tam, H.B. Cheng, Z.C. Dong, Peano-like paths for subaperture polishing of optical aspherical surfaces, Applied Optics 52 (15) (2013) 3624-3636.
37. C.R. Dunn, D.D. Walker, Pseudo-random tool paths for CNC sub-aperture polishing and other applications, Optics Express 16 (23) (2008) 18942-18949.
38. C.J. Wang, Z.Z. Wang, Q. Xu, Unicursal random maze tool path for computer-controlled optical surfacing, Applied Optics 54 (34) (2015) 10128-10136.
39. P.J. Best, N.D. McKay, A method for registration of 3-D shapes, IEEE Transactions on pattern analysis and machine intelligence 14 (2) (1992) 239-256.